Transmission Electron Microscope imaging sharpens geochronological interpretation of zircon and monazite

Anne-Magali Seydoux-Guillaume, Bernard Bingen, Valérie Bosse, Emilie Janots, Antonin Laurent

Transmission Electron Microscope imaging sharpens geochronological interpretation of zircon and monazite

Anne-Magali Seydoux-Guillaume[1, 2], Bernard Bingen[3], Valérie Bosse[1], Emilie Janots[4], and Antonin T. Laurent[2]

[1] *Laboratoire Magmas et Volcans, LMV UMR 6524 CNRS, UBP, IRD, Université Blaise Pascal, Clermont-Ferrand, France*

[2] *Université Lyon, UJM-Saint-Etienne, UBP, CNRS, IRD, Laboratoire Magmas et Volcans UMR 6524, Saint Etienne, France*

[3] *Geological Survey of Norway, 7491 Trondheim, Norway*

[4] *ISTerre, University Grenoble Alpes, Grenoble, France*

Keypoints:

1- Geochronological interpretations benefits from nanoscale characterization of zircon and monazite.

2- TEM provides evidences of the mechanisms behind disturbance of the U–Th–Pb geochronological systems resulting is discordant ages.

3- Nano-petrochronology improves the geochronological data interpretation on concordant dates spreading along the concordia curve.

Abstract

The present paper highlights the benefits of nanoscale characterization of the most commonly used minerals – zircon and monazite – in U–Th–Pb geochronology to sharpen

geochronological interpretations and convert isotopic ratios - a "date" - into a geologically meaningful age. Transmission Electron Microscopy (TEM) is a powerful analytical tool, and sometimes the only one, that can provide evidence of the mechanisms behind disturbance of the geochronological systems leading to discordance. These mechanisms include (1) distinct episodes of growth/replacement, (2) U, Th or Pb mobility (enhanced by the presence of nano-structural defects), (3) nano-inclusions or nano-chemical heterogeneity. Furthermore, TEM also helps to interpret concordant dates spreading along the Concordia curve. Such spread could represent protracted continuous growth, episodic short-duration growth, or U–Th–Pb disturbance of the geochronometers. In this paper, we show TEM images of nano-inclusions interfering with U–Th–Pb systematics and discuss how to address the impact of nano-inclusions on isotopic dates. Second, we show how experimental studies can be used to understand the mechanism of U–Th–Pb resetting in monazite. Finally, the third part focuses on nano-petrochronology of monazite, i.e. how the identification of nano-chemical tracer revealed by TEM improves the geochronological data interpretation.

Keywords: nanoscale characterization; linking TEM and U–Th–Pb geochronology; resetting mechanism; zircon and monazite; nano-petrochronology

1. Introduction

The orthosilicate zircon ($ZrSiO_4$) and orthophosphate monazite (Light Rare Earth Element phosphate: $LREEPO_4$) are the most widely used minerals in U–Pb and U–Th–Pb (only for monazite) geochronology in a variety of geological contexts [Parrish 1990; Harrison et al., 2002; Harley and Kelly, 2007; Corfu, 2013]. Ideally, the two decay chains, $^{238}U/^{206}Pb$, $^{235}U/^{207}Pb$, (and also the third one $^{232}Th/^{208}Pb$ in the case of monazite), yield concordant dates,

that are straightforwardly interpreted as the age of the zircon or monazite crystallization. However, discordant dates are frequent and indicate disturbance of the isotopic systems after initial crystallization. Yet, even in cases where the U–Pb data are entirely concordant, age disturbance cannot be ruled out (e.g. Ashwal et al., 1999). In a specific example from a monazite megacrystal from Arendal, Norway, high-resolution mineral characterization, in particular TEM, revealed partial replacement of primary monazite by secondary monazite due to late-stage alteration [Seydoux-Guillaume et al., 2007 and 2012]. In the secondary altered domains, *in-situ* U–Pb dating leads to concordant dates but meaningless ages, generally older than the primary material, due to contrasting U, Th and Pb redistribution during alteration. Sometimes, redistribution of the parent elements (U, Th), and radiogenic or non-radiogenic Pb takes place during the history of the mineral, leading to uncertain interpretation [Harrison et al., 2002; Villa and Williams, 2013]. Two critical processes are responsible for U–Th–Pb mobility and thus resetting in minerals: chemical reactions and diffusion [Cole and Chakraborty, 2001]. The relative efficiency and interplay of each of these processes depends mainly on temperature, time, grain-size or surface area, structural state of the lattice (defects induced by deformation and/or radiation damage) and presence of fluid or melt. The response of zircon and monazite to these parameters is briefly examined below.

Zircon is generally reactive (new domains with a size > 10's micrometer) in amphibolite-facies metamorphic conditions and beyond [Yakymchuk and Brown, 2014; DesOrmeau et al., 2015; Marsh and Stockli, 2015]. While solid state diffusion can be excluded in well crystallized zircon [Lee et al., 1997; Cherniak and Watson, 2003], zircon Achilles' heel is clearly the accumulation of radiation damage over time, critically affecting zircon physical and chemical properties. Typically, zircon contains U in the hundreds of ppm range, and consequently has received alpha-decay doses on the order of 10^{18}-10^{19} α/g and is easily amorphized [Ewing et al., 2000; Ewing et al., 2003]. Self-irradiation enhances diffusion

[e.g. Cherniak and Watson, 2003], facilitates mineral–fluid interaction [e.g. Geisler et al., 2003 and 2007; Nasdala et al., 2010], may lead to possible reduction of $Pb^{4+}$to Pb^{2+} [Kramers et al. 2009; Tanaka et al., 2010; Kogawa et al., 2012], and more generally can result in open system behavior even at low temperature (<200°C) and discordance [e.g. Geisler et al., 2007; Xu et al., 2012].

In contrast to zircon, the lattice of monazite is not affected by amorphization over time, in spite of alpha decay doses in the range of 10^{19}-10^{20} α/g, generated by extremely high concentrations of Th (up to 25 wt% ThO_2) and to a lower extent of U (up to 1 wt% UO_2) [Seydoux-Guillaume et al., 2004]. Clear evidence of radiation damage is limited to isolated nm-sized domains within monazite crystal. Mottled diffraction contrast in TEM is a very characteristic feature of monazite, resulting from a mosaic structure of the crystal, i.e., a lattice comprising many smaller domains with slightly different orientations. [Black et al., 1984; Meldrum et al., 1998; Seydoux-Guillaume et al., 2002b; 2003; 2004]. Solid-state diffusion of U, Th and Pb is insignificant up to high temperature conditions [Cherniak et al., 2004; Gardés et al., 2006; Gardés et al., 2007] and monazite can therefore yield precise ages without any isotopic disturbances after crystallization, at least under most crustal conditions. However, monazite is well known for its reactivity in the presence of fluids, even at low temperature [e.g. Poitrasson et al., 1996; 2000; Rasmussen et al., 2001; Bollinger and Janots, 2006; Janots et al., 2006; 2008; 2011; Seydoux-Guillaume et al., 2012; Allaz et al., 2013; Didier et al., 2013]. Commonly monazite crystals show patchy compositional zoning. Each zone corresponds to a distinct crystallization event recording changes that took place during the history of the host rock. These changes can be metamorphic solid-state reactions [e.g. destabilization of feldspar, crystallization of garnet; e.g. Rubatto et al., 2001], reaction with a silicate melt, fluid-rock interaction during alteration, metamorphism or metasomatism [e.g. Heinrich et al., 1997; Finger and Krenn 2007; Harlov et al., 2011; Janots et al., 2012; Didier et

al., 2013; Gauthiez-Putallaz et al., 2016], or dynamic recrystallization in response to deformation event [Erickson et al., 2015 and 2016]. This reactivity of monazite covers a large range of P-T-fluids conditions [Spear and Pyle, 2002] ranging from low grade metamorphism [Rasmussen and Muhling, 2007; Janots et al., 2006; 2008; 2011], granulite-facies metamorphism [Kelly et al., 2012; Kirkland et al., 2016], to magmatic conditions [Rubatto et al., 2013; Dumond et al., 2015; Wang et al., 2015]. In monazite, complex compositional zoning attests to successive crystallization events, either growth of new monazite and/or replacement of a previous one. These zones can be dated individually using microanalytical methods - Electron Microprobe analysis (EPMA), Secondary Ion Mass Spectrometry (SIMS), or Laser Ablation Inductively Coupled Plasma Mass Spectrometry (LA-ICP-MS) - and used to reconstruct the reaction history of the rock [e.g. Williams et al., 1999; 2007; 2012; Janots et al., 2012; Kelly et al., 2012].

The steady development in micro-sampling methods (SIMS, LA-ICP-MS, EPMA), now routinely applied for *in situ* dating of zircon and monazite, requires clear evaluation of the balance between analytical precision, analytical volume and effective volume of closed system behavior of the isotopic systems [Corfu, 2013; Nemchin et al., 2013; Schoene et al., 2013]. Any mobility of U, Th or Pb at a significant scale relative to the analytical volume or any overlap of the analytical volume between two volumes characterized by distinct isotopic closure leads to a disturbance, a modification of the initial crystallization age, or an analytically induced mixed age. In this context, Corfu [2013], based on the results of Moser et al. [2009], showed the benefit applying several analytical methods, with contrasted precision and microsampling performances, on the same geochronological problem, to provide arguments for correct interpretation of the data. In that specific case, the more precise ID-TIMS data are discordant but plot on a discordia line, whereas the less precise SIMS data all overlap the Concordia curve within error. Nano-petrochronology, is the characterization of

samples at different scales, including the nanometer scale [Kusiak et al., 2015; Seydoux-Guillaume et al., 2012 and 2015; Didier et al., 2015; Darling et al., 2016] or even atomic scale [Valley et al., 2014; Valley et al., 2015; Peterman et al., 2016; Piazolo et al., 2016] in order to link the mineral properties (nanostructure and nanoscale compositional heterogeneities) with geochronological data. Because Transmission Electron Microscopy (TEM) is the only technique able to combine nano-structural and nano-chemical information, it can provide evidences for the resetting mechanism of geochronological systems by identifying remnant of chemical reactions (e.g. secondary grains products and nano-inclusions; coupled dissolution-precipitation interface; pore filled with fluid/mineral/melt) or structural defects enhancing diffusion and alteration processes (e.g. amorphisation, plastic deformation). Insights from nano-characterization thus help to validate or invalidate the interpretation of an isotopic ratio (a "date") into a geologically meaningful age. In the case of mineral replacement, it is common that the replaced domain contained tiny crystals (micrometric to nanometric) of distinct mineral phases [Figure 1 and review in Putnis, 2009]. For example, the presence of nanocrystals of thorite ($ThSiO_4$) in apatite (Figure 1A-B) or uraninite (UO_2) in zircon (Figure 1C) compromises U–Th–Pb or U–Th/He dating. In the presence of fluid, primary monazite can react to form a secondary, Th–U-depleted monazite, typically accompanied by numerous thorite/huttonite ($ThSiO_4$) and/or thorianite (ThO_2) inclusions [Hetherington and Harlov, 2008; Seydoux-Guillaume et al., 2012; Figure 1D]. In inclusion-rich altered domains, inaccurate ages, measured by EPMA or LA-ICP-MS, results from the presence of numerous nano-phases and nano-fractures filled with Th–U-silicates that are visible only under TEM [Seydoux-Guillaume et al., 2012; Figure 1D]. Information coming from such nano-characterization may, however, help to improve the interpretation of dates. In this paper, we focus on zircon and monazite characterization with TEM and how it can sharpen interpretation of U–Th–Pb geochronological data. The paper is divided in three parts: the first

part presents examples of nano-inclusions that interfere with the U–Th–Pb systematics and how we can address them; the second part is dedicated to experimental studies and how they simulate the resetting of the U–Th–Pb systems in monazite; and the third part focuses on a micro- to nano-chemical tracer that may help to improve the interpretation of geochronological data.

2. Sample preparation.

Because TEM requires very thin samples, less than 100 nm thick, sample preparation for TEM characterization is one critical and essential step to obtain reliable analyzes. The development of the Focused Ion Beam (FIB) technique for TEM preparation has considerably opened the possibilities for TEM characterization, especially for the geoscience community, for which imaging of tiny phases or inclusions, microstructures or interfaces *in situ*, in their thin section context, is often crucial. The FIB preparation allows to produce site-specific TEM foils, typically 10-15 µm large over 5-10 µm in depth and less than 0.1 µm thick slice, cut perpendicular to the surface of a (c. 30µm thick) petrographic thin section. The FIB is the sole technique that allows cutting TEM-ready foils with homogeneous sample thickness, in a section from a well-defined area such as mineral boundary, without preferential thinning or production of artifacts. Many examples and details of the technique are reviewed in Wirth [2004 and 2009]. Nowadays, most of the TEM studies are closely associated and dependent from FIB preparations.

3. Structural and chemical evidence for nano-inclusions affecting the U–Th–Pb systematics in monazite and zircon.

3.1. Zircon

Heterogeneous distribution of radiogenic Pb in zircon at sub-micrometer scale was first identified by High-Angle Annular Dark Field Scanning Transmission Electron Microscope- (STEM-HAADF) imaging [Utsunomiya et al., 2004]. The authors found nanoscale patches rich in Pb in two locations: inside the zircon lattice (concentrated at 3 at%) and inside amorphous domains from fission tracks. They suggested that beyond the first percolation point [Salje et al., 1999; Trachenko et al., 2003; Geisler et al., 2007], when amorphous domains overlap and form an interconnected network, Pb will diffuse faster in zircon. These observations were confirmed a few years later by Utsunomiya et al. [2007] using the same technique. Even if the first percolation point will differ a little depending on the thermal history of the sample [Geisler et al., 2003], the dose is estimated to be of 2.2 x 10^{18} α/g [Pidgeon, 2014]. Beyond the first percolation point, the probability of enhanced Pb mobility in response to an external event, like for example metamorphism, is very high.

Lead mobility in polymetamorphic zircon of the Napier complex of Enderby Land, Antarctica, was documented earlier through SIMS micro-analysis by Black et al. [1986]. In the same sample, these authors observed reverse and normal discordance of the U–Pb isotopic system, attesting for Pb mobility with simultaneous Pb loss or Pb gain depending on the analytical spot. The nature and size of isotopic perturbation in high-grade polymetamorphic samples were recently addressed using SIMS imaging [Kusiak et al., 2013; Whitehouse et al., 2014], and TEM [Kusiak et al., 2015]. Thanks to HAADF-TEM and electron diffraction patterns, Kusiak et al. [2015] identified nanospheres of metallic Pb, 5 to 30 nm in diameter, randomly distributed in those zircons (Figure 2C-D). The nanospheres are commonly associated with an amorphous silica-rich phase and Ti- and Al-rich phases, interpreted to be melt inclusions formed during ultra-high temperature metamorphism. The patchy-distribution of Pb highlighted with SIMS imaging [Kusiak et al., 2013; Figure 2B] causes the spreading of discordance and U–Pb ages (Figure 2A), and can be attributed to the presence of metallic Pb-

nanospheres in zircon [Kusiak et al., 2015]. Identification (type of phase, structure, size, morphology) of these nanospheres was feasible thanks to the combination of nano-structural and nano-chemical analyzes, only achievable with TEM. In contrast, the Atom Probe Tomography (APT) would not provide structural information, and would only reveal the presence of Pb-nanoclusters and their isotopic composition [e.g. Peterman et al., 2016; Piazolo et al., 2016]. Their metallic nature can only be determined using nano-diffraction with TEM [Kusiak et al., 2015]. In this example, TEM characterization helps to prove that apparent ages as old as 4.2 Ga do not correspond to relicts of ancient zircons (and thus have no geological meaning), but to Pb migration and coalescence into Pb metallic nanosphere during the recovery of crystallinity in radiation-damaged zircon under high-grade metamorphism [Kusiak et al., 2015]. Such redistribution of radiogenic Pb at the nanoscale may compromise the precision and accuracy of U–Pb obtained by high-resolution *in situ* methods like SIMS, as shown by Kusiak et al., [2013] and Whitehouse et al. [2014]. When larger analytical volumes are considered (e.g. by LA-ICP-MS or SIMS), the effect of the nanoscale heterogeneities may decrease. In Kusiak et al. [2013], the dates obtained with the highest spatial resolution (2 µm) generates meaningless age up to 4198 Ma [Figure 2B], whereas analyzes with typical SIMS spot size of c. 15µm yield broad distribution of ages between 3324 and 3605 Ma [Figure 3F in Kusiak et al., 2013]. This leads thus to the question of what should be the optimal spatial resolution for *in situ* analyses?

Mobility of the parent element U in zircon has also been documented by Seydoux-Guillaume et al., [2015] using STEM-HAADF and STEM-Energy Dispersive X-Ray Spectroscopy (EDS) analyses coupled with U–Pb isotopic analysis. In a pegmatite from Norway [Duran et al., 2016], atypical zircon phenocrysts are affected by intense self-irradiation, associated with amorphization, microporosity, swelling, radial cracking, and uptake of non-formula cations like Ca. Fractures and pores represent the vectors for fluid

mediated open system behavior. This alteration leads to increased discordance of the U–Pb system (Figure 3A-B). Again, STEM (HAADF and EDS) analyses demonstrate the presence of U-rich (uraninite) clusters (<70 nm) within the porosity and of high density walls (<50 nm), enriched in U or Ca or both, coating the pores (Figure 3C-D). It is only the close association of nano- characterization (TEM) to the geochronological data [Seydoux-Guillaume et al., 2015; Figure 3] that allows to interpret the spatial link between U, Ca and porosity as evidence for U uptake, and which demonstrates that discordance of the U–Pb system in zircon affected by radiation damage includes a component of U- mobility (U-gain - U-loss).

Both examples by Kusiak et al., [2015] and Seydoux-Guillaume et al., [2015] are notes of the promising role of nano-petrochronology for geochronological studies, especially when ages are discordant. They demonstrate how careful nano-scale characterization, associating the U–Pb analytical data with their structural context, may avoid spurious age interpretation. A meaningful age cannot be extracted from all zircon grains, because some are likely to be affected by radiation damage and/or chemical reactions, which will cause and enhance Pb and U mobility.

3.2. Monazite

Monazite is much less studied than zircon and, as far as we know, few studies attempted to link TEM characterization to geochronological interpretation. Black et al. [1984] focused on monazite from polymetamorphic rocks of the Napier complex in Antarctica. The authors tried to link the color of monazite grains (brown, yellow and grey) with the nanostructure (TEM) and the discordance. Independently of the color, all monazite crystals present the same nanostructure, i.e. 100 Å crystalline domains misoriented from each other by

246 no more than 2 x 10^{-3} radians, leading to mottled diffraction contrasts on Bright Field or Dark
247 Field (BF/DF)-TEM images. Such observation is typical for monazite crystals and the mottled
248 contrast is attributed to radiation damage and was confirmed later by Seydoux-Guillaume et
249 al. [2004] in a comparison between different monazite samples (from 24 Ma to 2 Ga). To
250 address the problem of inconsistent electron-microprobe (EPMA) chemical ages in complex
251 monazite from a polymetamorphic granulite (Andriamena unit, Madagascar, Seydoux-
252 Guillaume et al. [2003] linked a TEM study with electron-microprobe U–Th–Pb chemical
253 dating. The presence of 50nm Pb-rich inclusions is revealed in monazite domains where large
254 variations in EPMA dates are detected (Figure 4). The nature of these inclusions is not
255 completely understood, but it was proposed that they could be a Pb-Ca-Si-O phase like
256 margarosanite ($Ca_2PbSi_3O_9$) or more probably represent material that crystallized in fluid
257 inclusions (Figure 4B-C). The TEM study led to a new interpretation of EPMA dates for
258 monazite previously considered to be the result of partial Pb loss from a 2.5 Ga monazite. The
259 scatter of apparent ages ranging from 2.5 Ga to 790 Ma (Figure 4A) is reinterpreted to result
260 from the replacement of a primary monazite by a secondary monazite during a metamorphic
261 event at 790 Ma with random incorporation of various amount of Pb-rich inclusions in the
262 analytical volume of the EPMA analysis in secondary monazite domains. The presence of Pb-
263 rich inclusions suggests that recrystallization of monazite does not result, in this case, in a
264 total removal of previously accumulated radiogenic Pb, but partial preservation in Pb-rich
265 clusters. This study therefore exemplifies that domains of unsupported Pb can exist in
266 monazite. This result was recently confirmed by several studies [e.g. Seydoux-Guillaume et
267 al., 2012; Didier et al., 2013], that also suggest that Pb-rich nano-inclusions (or nano-
268 domains) could contain a non-radiogenic Pb component.

269

4. Nanoscale constrains on the resetting mechanism of U–Th–Pb systems in experimentally altered monazite.

The first experimental study addressing the hydrothermal resetting of the U–Pb systems in monazite was performed in 1997 by Teufel and Heinrich [1997] in pure water. Partial resetting of the U–Pb systems was evaluated by multigrain ID-TIMS analysis of the experimental products. Partial resetting was only detected for a starting material made of fine monazite powder (<1-15µm) and could be shown to be the result of monazite dissolution and precipitation of neoformed monazite. The maximum Pb loss of 26% (ID-TIMS dating of the experimental product) was observed at the highest temperature (750°C). A major revelation of this study was that dissolution and precipitation is more efficient than volume diffusion [Cherniak et al., 2004; Gardès et al., 2006 and 2007] to reset the U–Pb clock in monazite. Seydoux-Guillaume et al. [2002], confirmed the importance of the dissolution-precipitation mechanism by performing a series of experiments (800-1200°C) using different fluid compositions. Monograins (200-400µm) of the experimental products were analyzed by ID-TIMS, EPMA and SIMS show that 1) partial resetting was obtained only in the presence of Ca-rich fluid at 1000°C and involved dissolution followed by precipitation of Pb-free neoformed monazite; 2) experiments with Pb-bearing fluid produced sub-concordant monazite for which the $^{207}Pb/^{206}Pb$ apparent ages were older than the primary monazite used for the experiment, demonstrating that monazite may incorporate Pb from a fluid. This last result is consistent with TEM observations by Seydoux-Guillaume et al. [2003] that Pb-rich nano-domains observed in monazite samples from Madagascar may be incorporated from a fluid phase and may explain contamination by common Pb recorded in some natural monazites [e.g. Didier et al., 2013; Janots et al., 2012; Seydoux-Guillaume et al., 2012].

Based on natural observations that metasomatic alteration of monazite is particularly developed in Na- and K-rich geological environments [Harlov et al., 2007; Hetherington and

295 Harlov, 2008], monazite alteration experiments were performed in the presence of Na- or K-
296 rich fluids, with different ligands, starting material and temperature [Harlov and Hetherington,
297 2010; Hetherington et al., 2010; Harlov et al., 2011; Williams et al., 2011; Budzyn et al.,
298 2011; 2015; Shazia et al., 2016]. All these experimental studies show that alkali fluids are the
299 most efficient fluids to promote monazite replacement, even for temperature as low as 250°C
300 [Budzyn et al., 2016]. Under these conditions, the monazite texture of experimentally
301 replaced monazite is typical of those encountered in natural systems. It shows a secondary
302 rim, that is normally porous, and with a composition that differs of the original monazite
303 starting material. This replacement process is now believed to be preponderant in numerous
304 natural environments (diagenetic, metamorphic or hydrothermal).

305 Using TEM characterization, Harlov et al. [2011] could demonstrate that the
306 replacement of experimental products is caused by an interfacially coupled dissolution-
307 precipitation mechanism [e.g. Putnis and Putnis, 2007; Putnis 2009]. Indeed, TEM
308 observations reveal a sharp reaction interface between primary domains (starting material
309 with radiation damage) and secondary domains free of radiation damage, with negligible
310 evidence of diffusion even at the nanoscale. These experimental studies also indicate that the
311 physicochemical conditions of the fluid play an important role on the U–Th–Pb resetting in
312 secondary monazite. Remarkably, the U–Th–Pb system is not systematically reset and Pb is
313 present in altered domain produced in presence of NaOH or KOH fluids [Harlov et al., 2011]
314 or Na_2SiO_5 bearing fluids below 350°C [Budzyn et al., 2015]. However, Pb was close or
315 below the detection limit in monazite altered domain produced in presence of Na_2SiO_5
316 bearing fluids at 450°C [Williams et al., 2011] or in presence of K- and Na-rich melts at
317 800°C [Shazia et al., 2016]. As a consequence such altered chemical domains may be dated
318 by in situ techniques [EPMA in Williams et al., 2011] and thus offer a great potential to date
319 metasomatic events.

320 Recently, progress done on high spatial resolution *in situ* analytical techniques (e.g.
321 LA-ICP-MS), and on the development of site specific preparation (FIB-Focused Ion Beam)
322 for TEM analyses, allow Grand'Homme et al., [2016b] to formulate a new hypothesis to
323 explain partial resetting observed in experimentally altered monazite samples (300-600°C)
324 under alkali conditions. Experimentally altered monazite rims (Figure 5B; at 500°C), dated
325 using *in situ* techniques (EPMA and LA-ICP-MS) systematically yield intermediate dates
326 (Figure 5A; EPMA) between pristine monazite (555 Ma) and complete experimental resetting
327 (0 Ma), with a mean date that decreases with increasing temperatures (down to 71 ± 27 Ma at
328 600°C). Nanometric characterizations using TEM of experimental products elucidated the
329 origin of this partial resetting. At such nanoscale, the replacement is incomplete within the
330 altered rim (Figure 5C): altered rim corresponds to a nano-mixture of Pb-free (EDS-TEM)
331 secondary monazite (mnz2), with inherited monazite (mnz1). No Pb-bearing inclusions were
332 observed in the altered domain. The partial resetting depends then on the nano-mixture of
333 different proportion of mnz1 in the analyzed volume (Figure 5C). Even in the case of EPMA
334 analyses, where the interaction volume is the smallest (< 35 μm^3; but with no way to have a
335 3D control during the analysis), a scattering of dates exists and lead to erroneous ages (Figure
336 5A; 163 ± 54 Ma at 500°C). Partial replacement in altered domains certainly applies to
337 monazite naturally replaced in the presence of fluid. Indeed, the experimental results simulate
338 well the microstructures of fluid-driven replacements (skeletal structures, microporosity,
339 inclusion) and can account for the age scattering and discordance obtained in altered monazite
340 domains [e.g., Bosse et al., 2009; Kelly et al., 2012; Seydoux-Guillaume et al., 2012; Didier et
341 al., 2013; Grand'Homme et al., 2016a] but also in rock deformed by dislocation creep, where
342 incomplete resetting was proposed but not explained [e.g. Wawrzenitz et al., 2012; Erickson
343 et al., 2015 and 2016]. However, in the case of new monazite (over)growths involving
344 spatially decoupled dissolution and precipitation [e.g. dissolution-precipitation creep in

345 deformed rock; Wawrzenitz et al., 2012; Didier et al., 2014; Erickson et al., 2015 and 2016]
346 and experimentally reproduced in Seydoux-Guillaume et al. [2002], such nano-scale
347 incomplete replacement will not occur. It may be challenging to recognize possible
348 disturbances linked with nanomixture, when large age data sets are determined with no
349 reliable micro (to nano)-textural documentation on the dated grains (e.g., as for example in
350 provenance studies).

351

352 **5. Nano-petrochronology of monazite.**

353 The structural flexibility of monazite permits substitution of more than 25 elements of
354 the periodic table in its lattice [Clavier et al., 2011]. Monazite is monoclinic with space group
355 P21/n and its structure is organized in chains, parallel to c-axis, with alternating PO_4
356 tetrahedrons and $REEO_9$ polyhedrons [Ni et al., 1995; Boatner, 2002; Clavier et al., 2011].
357 The nine-fold site preferentially incorporates LREE, but may accommodate a large variety of
358 other (possibly larger) cations, especially Th, U, and Ca by two well-documented substitution
359 types [Förster, 1998; Montel et al., 2002; Clavier et al., 2011]. The cheralite [$CaTh(PO_4)_2$;
360 formerly called brabantite] exchange $An^{4+} + M^{2+} = 2REE^{3+}$ - with An = (Th, U) and M = (Ca,
361 Ba, Sr, Pb) - involving the nine-fold site alone and the huttonite ($ThSiO_4$) exchange $An^{4+} +$
362 $Si^{4+} = 2REE^{3+} + P^{5+}$ that involve both sites. Furthermore, Y and HREE are incorporated
363 through the xenotime (YPO_4) substitution; this property allows monazite to be used as a
364 thermometer when associated with xenotime [Gratz and Heinrich, 1997; Heinrich et al., 1997;
365 Seydoux-Guillaume et al., 2002b] and with garnet [Pyle et al., 2001]. More exotic cations
366 may be incorporated into monazite lattice; these include S incorporated as anhydrite
367 component [$CaSO_4$; Chakhmouradian and Mitchell, 1999; Prsek et al. 2010; Krenn et al.,
368 2011], Sr [Krenn et al., 2011; Holder et al., 2015; Prsek et al. 2010], As incorporated as a
369 gasparite component [$CeAsO_4$; Ondrejka et al., 2007; Janots et al., 2006; 2008; 2011; Gnos et

al., 2015], and V [McFarlane and McKeough, 2013]. The structural incorporation of redox-sensitive elements in monazite opens the perspective of tracing the evolution of the oxidation state through time in a large number of rocks, thanks to the U–Pb and Th–Pb isotopic systems.

To show the importance of sulfur as a petrogenetic tracer and the contribution of TEM imaging to uncover it, we focus here on complexly patchy zoned monazite crystals (Figure 6A) from an osumilite-bearing granulite from Rogaland, Norway [Laurent et al., 2016], in which *in situ* U–Pb dating (LA-ICP-MS) were performed (Figure 6B). The U–Pb dataset of monazite is concordant to sub-concordant (conc. > 95 %), with analyses plotting continuously along the concordia curve from ca. 1040 Ma down to 920 Ma (Figure 6B). When considering the chemical composition at both micro- and nano-scale (Figures 6E-F), more specific and useful information can be extracted to interpret the apparently continuous age spread. In the monazite crystals, three chemical domains are distinguished (Figure 6A, C-D): D1, a S-rich core (0.45–0.72 Wt. % SO_2-Figure 6D, Th incorporated as cheralite component, i.e. Si-poor Figure 6C), D2, secondary S-bearing domains (SO_2> 0.05 Wt. %, partly clouded with solid inclusions-Figure 6A), and D3, late S-free-Figure 6D, Y-rich, domains (0.8–2.5 Wt. % Y_2O_3, Th accommodated as huttonite component, i.e. Si-rich Figure 6C). Nano-characterization of the S-rich monazite domains (D1), using FIB preparation coupled with STEM-HAADF imaging, revealed the presence of black dots (5-10 nm in size) homogenously distributed all over the foil and representing negative density contrast in monazite (arrow in Figure 6E). High resolution STEM-HAADF image (Figure 6F) demonstrates that these nanoclusters are made of anhydrite ($CaSO_4$) characterized by a coherent interface toward the host monazite. These data imply that S was incorporated in the monazite lattice as a clino-anhydrite component following the exchange $Ca^{2+}+S^{6+}=REE^{3+}+P^{5+}$, but then is partly exsolved in nanoclusters of $CaSO_4$. Monazite with significant sulfate substitution is expected to crystallize

from oxidized geological fluids or melts in which sulfur is present as S^{6+}. The close combination of micro-chemical (EPMA) and nano-structural and nano-chemical (STEM) analyses with U–Pb dating allow to attribute precise ages to these three domains. The S-rich core D1 yields a concordia age of 1034 ± 6 Ma, S-bearing D2 gives a significantly younger age of 1005 ± 7 Ma and S-free D3 of 935 ± 7 Ma (Figures C-D). From regional correlation [Bingen et al., 2008] and sulphide phase-stability diagrams [Whitney et al., 1984], the interpretation is that S-rich monazite cores (D1) crystallized at 1034 ± 6 Ma from an oxidized, sulphate (S^{6+})-dominated granitic melt during fluid-absent partial melting. Monazite may therefore be used to probe the presence of sulfur in anatectic melts from high-grade terrains at a specific point in time and date sulfur mobilization from reduced to oxidized state. This interpretation could be provided only because TEM analyses proves that sulfur substitutes as $CaSO_4$ in monazite lattice, and not as inclusions that may reflect and record other processes than primary crystallization [e.g. in figure 6A, sulfur inclusions in D2 reflect metasomatism event; monazite inclusions in Rasmussen et al., 2011 record metamorphic event).

6. Conclusions

This paper highlights how characterization at the nanoscale, with combination of nano-structural and nano-chemical information, using TEM, provides insights to understand the U–Th–Pb systematics of zircon and monazite and improve age geochronological interpretations. This nano- scale characterization, referred as nano-petrochronology, provides information not only on perturbation of the isotopic systems, but it also contributes to understand reaction mechanisms and distribution of petrogenetically important trace elements. This is well illustrated by the input of nano-chemical tracer ($CaSO_4$) in monazite or by the presence of Pb or U rich-nanophases in monazite and zircon crystals. This nano-

419 petrochronology approach could possibly applied to other common U–Th–Pb chronometers
420 (i.e. titanite, allanite).

421 The paper also raises the question of the optimal spatial resolution for *in situ* analyses,
422 a critical issue coming from the improvement of the *in situ* analytical techniques (e.g. LA-
423 ICP-MS, HR-SIMS, nano-SIMS, EPMA) and well-demonstrated by the studies of Kusiak et
424 al. [2013] and Valley et al. [2014] for zircon, or Seydoux-Guillaume et al. [2003] and [2012]
425 for monazite. We suggest that the use of high-spatially resolved techniques requires even
426 more careful nano-characterization (with TEM) of the samples, to provide reliable
427 geochronological interpretations of the data.

428 Furthermore, considering the complementarity of the Atom Probe Tomography (APT)
429 technique, which provides isotopic information within nanoscale domains [e.g. Valley et al.,
430 2014; Valley et al., 2015; Peterman et al., 2016; Piazolo et al., 2016] in typical analyzed
431 volumes of material of 50x50x200nm^3, we assert that combination of APT with TEM, a
432 highly complementary technique yielding both nano-structural and nano-chemical
433 information, would considerably improve the interpretation of U–Th–Pb geochronological
434 data; such correlative microscopy should certainly be developed in the future.

435 The need of experimental data has been demonstrated, in order to better constrain the
436 behavior of parent (e.g. U, Th) and daughter (e.g. Pb) elements and the resetting mechanisms
437 under a large range of conditions (P-T-fluids). Indeed, it has been demonstrated for monazite,
438 that incomplete replacement at the nanoscale may lead to partial resetting of the U–Th–Pb
439 systems and thus to meaningless ages. Such experimental studies coupling nano-
440 characterization with the behavior of isotopic systems (U–Pb but also Lu–Hf) are long
441 overdue for zircon, and, in contrast to monazite, certainly highly dependent on its structural
442 state due to its sensitivity to radiation damage [Geisler et al., 2007].

Acknowledgement

The authors thank L. Datas (UMS Castaing, Toulouse), C. Dominici (CP2M-Marseille) and B. Reig (LAAS, Toulouse) for technical assistance. The paper benefited from insightful discussions with many of our students, colleagues, and friends including Amélie Didier, Stéphanie Duchene, Charley Duran, Philippe Goncalves, Alexis Grand'homme, Damien Guillaume, Simon Harley, Wilhelm Heinrich, Jean-Marc Montel, Jean-Louis Paquette, Franck Poitrasson, Andrew and Christine Putnis, and Richard Wirth. The French RENATECH network allows to prepare most of the FIB samples. Collaborations were promoted thanks to PHC Aurora (Ministry of Foreign affairs of France and the Research Council of Norway). Both the NEEDS (CNRS) French Research Group and the ANR-12-JS06–0001–01 (MONA) provided financial support. We thank Desmond Moser, Editor-in-Chief, S. Reddy, associate editor, A. Cavosie and an anonymous reviewer, whose comments significantly improved the paper.

References

Allaz, J., Selleck, B., Williams, M.L., and Jercinovic, M.J. (2013). Microprobe analysis and dating of monazite from the Potsdam Formation, New York: A progressive record of chemical reaction and fluid interaction. Am. Mineral. 98, 1106–1119.

Ashwal, L.D., Tucker, R.D., and Zinner, E.K. (1999). Slow cooling of deep crustal granulites and Pb-loss in zircon: Geochim. Cosmochim. Acta, 63, 2839-2851.

Bingen, B., Nordgulen, O., and Viola, G. (2008). A four-phase model for the Sveconorwegian orogeny, SW Scandinavia. Nor Geol Tidsskr, 88, 43.

Black, L.P., Fitzgerald, J.D., and Harley, S.L. (1984). Pb isotopic composition, colour, and microstructure of monazites from a polymetamorphic rock in Antarctica. Contrib. Mineral. Petrol., 85, 141-148.

469 Black, L. P., Williams, I. S., and Compston, W. (1986). Four zircon ages from one rock: the
470 history of a 3930 Ma-old granulite from Mount Sones, Enderby Land, Antarctica.
471 Contributions to Mineralogy and Petrology, 94, 427-437.

472 Boatner, L. (2002). Synthesis, Structure, and Properties of Monazite, Pretulite, and Xenotime.
473 In Reviews in Mineralogy and Geochemistry (ed. P. H. Ribbe) 48, pp. 87-121.
474 Mineralogical Society of America.

475 Bollinger, L., and Janots, E. (2006). Evidence for Mio-Pliocene retrograde monazite in the
476 Lesser Himalaya, far western Nepal. Eur. J. Mineral. 18, 289–297.

477 Bosse, V., Boulvais, P., Gautier, P., Tiepolo, M., Ruffet, G., Devidal, J.L., Cherneva, Z.,
478 Gerdjikov, I., and Paquette, J.L. (2009). Fluid-induced disturbance of the monazite Th-Pb
479 chronometer: In situ dating and element mapping in pegmatites from the Rhodope (Greece,
480 Bulgaria). Chem. Geol., 261, p. 286-302.

481 Budzyn, B., Harlov, D.E., Williams, M.L., and Jercinovic, M.J. (2011). Experimental
482 determination of stability relations between monazite, fluorapatite, allanite, and REE-
483 epidote as a function of pressure, temperature, and fluid composition. Am. Mineral. 96,
484 1547–1567.

485 Budzyn, B., Jastrzebski, M., Kozub-Budzyn, G.A., and Konecny, P. (2015). Monazite Th-U-
486 total Pb geochronology and P-T thermodynamic modelling in a revision of the HP-HT
487 metamorphic record in granulites from Stary Gieraltow (NE Orlica-Snieznik Dome, SW
488 Poland). Geol. Q. 59, 700–717.

489 Chakhmouradian, A.R., and Mitchell, R.H. (1999). Niobian ilmenite, hydroxylapatite and
490 sulfatian monazite: alternative hosts for incompatible elements in calcite kimberlite from
491 Internatsional'naya, Yakutia. Can. Mineral. 37, 1177-1189.

492 Cherniak, D.J., Watson, E.B., 2003. Diffusion in zircon, in: Hanchar, J.M., Hoskin, P.W.O.
493 (Eds.), Zircon. Mineralogical Soc Amer, Chantilly, pp. 113–143.

494 Cherniak, D.J., Watson, E.B., Grove, M., Harrison, T.M. (2004). Pb diffusion in monazite: a
495 combined RBS/SIMS study. Geochim. Cosmochim. Acta, 68, 829-840.

496 Clavier, N., Podor, R., and Dacheux, N. (2011). Crystal chemistry of the monazite structure. J.
497 Eur. Cer. Soc., 31, 941-976.

Cole, D. R., & Chakraborty, S. (2001). Rates and mechanisms of isotopic exchange. Reviews in Mineralogy and Geochemistry, 43(1), 83-223.

Corfu, F. (2013). A century of U–Pb geochronology: the long quest towards concordance. Geol. Soc. Am. Bull., 125, 33-47.

Darling, J.R., Moser, D.E., Barker, I.R., Tait, K.T., Chamberlain, K.R., Schmitt, A.K., and Hyde, B.C. (2016). Variable microstructural response of baddeleyite to shock metamorphism in young basaltic shergottite NWA 5298 and improved U-Pb dating of Solar system events. Earth Planet. Sci. Lett., 444, 1-12.

DesOrmeau, J.W., Gordon, S.M., Kylander-Clark, A.R.C., Hacker, B.R., Bowring, S.A., Schoene, B., and Samperton, K.M. (2015). Insights into (U)HP metamorphism of the Western Gneiss Region, Norway: A high-spatial resolution and high-precision zircon study: Chem. Geol., 414, 138-155.

Didier, A., Bosse, V., Boulvais, P., Bouloton, J., Paquette, J.-L., Montel, J.-M., and Devidal, J.-L. (2013). Disturbance versus preservation of U–Th–Pb ages in monazite during fluid–rock interaction: textural, chemical and isotopic in situ study in microgranites (Velay Dome, France). Contrib. Mineral. Petrol., 165, 1051-1072.

Didier, A., Bosse, V., Cherneva, Z., Gautier, P., Georgieva, M., Paquette, J.L., and Gerdjikov, I. (2014) Syn-deformation fluid-assisted growth of monazite during renewed high-grade metamorphism in metapelites of the Central Rhodope (Bulgaria, Greece). Chem Geol 381:206–222

Didier, A., Bosse, V., Bouloton, J., Mostefaoui, S., Viala, M., Paquette, J.L., Devidal, J.L., and Duhamel R. (2015). NanoSIMS mapping and LA ICP MS chemical and U–Th–Pb data in monazite from a xenolith enclosed in ndesite (Central Slovakia Volcanic Field). Contrib. Mineral. Petrol., 170 doi:10.1007/s00410-015-1200-1.

Dumond, G, Goncalves, P, Williams, ML, and Jercinovic, MJ (2015). Monazite as a monitor of melting, garnet growth, and feldspar recrystallization in continental lower crust. J. Metamorph. Geol. doi: 10.1111/jmg.12150

Duran, C.J., Seydoux-Guillaume, A-M, Bingen, B., Gouy, S., de Parseval, P., Ingrin, J., and Guillaume, D. (2016). Fluid-mediated alteration of (Y,REE,U,Th)–(Nb,Ta,Ti) oxide minerals in granitic pegmatite from the Evje-Iveland district, southern Norway. Min. Petrol., DOI 10.1007/s00710-016-0436-4.

529 Erickson, T.M., Cavosie, A.J., Pearce, M.A., Timms, N.E., and Reddy, S. (2016). Empirical
530 constraints on shock features in monazite using shocked zircon inclusions. Geology, 44,
531 635-638.

532 Erickson, T.M., Pearce, M.A., Taylor, R.J.M., Timms, N.E., Clark, C., Reddy, S.M. and
533 Buick, I.S. (2015). Deformed monazite yields high-temperature tectonic ages. Geology, 44,
534 635-638

535 Ewing, R.C.,Meldrum, A.,Wang, L.M.,Wang, S.X. (2000): Radiation- induced amorphisation.
536 Rev. Mineral. Geochem., Ribbe P.H., ed., Mineral. Soc. Amer., Washington DC., 39, 319-
537 361.

538 Ewing, R.C., Meldrum, A., Wang, L.M., Weber, W.J., and Corrales, L.R. (2003). Radiation
539 damage in zircon. In: Hanchar, J.M., Hoskin, P.W.O. (Eds.), Zircon. In: Reviews in
540 Mineralogy and Geochemistry, vol.53. Mineralogical Society of America, 387-425.

541 Finger, F., and Krenn, E. (2007). Three metamorphic monazite generations in a high-pressure
542 rock from the Bohemian Massif and the potentially important role of apatite in stimulating
543 polyphase monazite growth along a PT loop. Lithos 95:103–115.

544 Förster, H.J. (1998): The chemical composition of REE-Y-Th-U rich accessory minerals in
545 peraluminous granites of the Erzgebirge-Fichtelgebirge region, Germany, Part I: The
546 monazite-(Ce)-brabantite solid solution series. Am. Mineral., 83, 259-272.

547 Gardés, E., Jaoul, O., Montel, J.-M., Seydoux-Guillaume, A.-M., and Wirth, R. (2006). Pb
548 diffusion in monazite: An experimental study of interdiffusion. Geochim. Cosmochim.
549 Acta, 70, 2325-2336.

550 Gardés, E., Montel, J.-M., Seydoux-Guillaume, A.M., and Wirth, R. (2007). Pb diffusion in
551 monazite: New constraints from the experimental study of Pb^{2+}=Ca^{2+} interdiffusion.
552 Geoch. et Cosmochim. Acta , 71, 4036-4043.

553 Gauthiez-Putallaz, L., Rubatto, D., and Hermann, J. (2016). Dating prograde fluid pulses
554 during subduction by in situ U–Pb and oxygen isotope analysis. Contrib. Mineral. Petrol.
555 171. doi:10.1007/s00410-015-1226-4

556 Geisler, T., Rashwan, A.A., Rahn, M.K.W., Poller, U., Zwingmann, H., Pidgeon, R.T.,
557 Schleicher, H., Tomaschek, F. (2003). Low temperature hydrothermal alteration of natural
558 metamict zircons from the Eastern Desert, Egypt. Mineral. Mag., 67, 485-508.

559 Geisler, T., Schaltegger, U., and Tomaschek, F. (2007). Re-equilibration of zircon in aqueous
560 fluids and melts. Elements, 3, 43–50.

561 Gnos, E., Janots, E., Berger, A., Whitehouse, M., Walter, F., Pettke, T., and Bergemann, C.
562 (2015). Age of cleft monazites in the eastern Tauern Window: constraints on
563 crystallization conditions of hydrothermal monazite. Swiss J. Geosci. 108, 55–74.

564 Grand'homme, A., Janots, E., Bosse, V., Seydoux-Guillaume, A.M., de Ascenção, G.
565 (2016a). Interpretation of Th-Pb and U-Pb in-situ ages of hydrothermal monazite:
566 Evidence from a large-scale regional study in clefts from the western Alps. Mineralogy and
567 Petrology doi:10.1007/s00710-016-0451-5.

568 Grand'Homme, A., Janots, E., Seydoux-Guillaume, A.-M., Guillaume, D., Bosse, V., and
569 Magnin, V. (2016b). Partial resetting of the U-Th-Pb systems in experimentally altered
570 monazite: Nanoscale evidence of incomplete replacement. Geology vol.44, p.439-442,
571 doi:10.1130/G37770.1.

572 Gratz, R., and Heinrich, W. (1997). Monazite-xenotime thermobarometry: experimental
573 calibration of the miscibility gap in the binary system $CePO_4$-YPO_4. Am. Mineral., 82,
574 772-780.

575 Harlov, D.E., and Hetherington, C.J. (2010). Partial high-grade alteration of monazite using
576 alkali-bearing fluids: Experiment and nature. Am. Mineral. 95, 1105–1108.

577 Harlov, D.E., Wirth, R., and Hetherington, C.J. (2011). Fluid-mediated partial alteration in
578 monazite: the role of coupled dissolution-reprecipitation in element redistribution and mass
579 transfer. Contrib. Mineral. Petrol. 162, 329–348.

580 Harrison, T.M., Catlos, E., and Montel, J.M. (2002). U-Th-. Pb dating of phosphate minerals.
581 In Reviews in Mineralogy and Geochemistry (ed. P. H. Ribbe) 48, pp. 523–558.
582 Mineralogical Society of America.

583 Heinrich, W., Andrehs, G., and Franz, G. (1997). Monazite–xenotime miscibility gap
584 thermometry. I. An empirical calibration. J. Metamorph. Geol., 15, 3-16.

585 Hetherington, C.J., and Harlov, D.E. (2008). Metasomatic thorite and uraninite inclusions in
586 xenotime and monazite from granitic pegmatites, Hidra anorthosite massif, southwestern
587 Norway: Mechanics and fluid chemistry: American Mineralogist, 93, 806-820.

588 Hetherington, C.J., Harlov, D.E., and Budzyn, B. (2010). Experimental metasomatism of
589 monazite and xenotime: mineral stability, REE mobility and fluid composition. Mineral.
590 Petrol. 99, 165–184.

591 Holder, R.M., Hacker, B.R., Kylander-Clark, A.R.C., and Cottle, J.M. (2015). Monazite trace-
592 element and isotopic signatures of (ultra) high-pressure metamorphism: examples from the
593 Western Gneiss Region, Norway. Chem. Geol., 409, 99-111.

594 Janots, E., Negro, F., Brunet, F., Goffé, B., Engi, M., and Bouybaouène, M.L. (2006).
595 Evolution of the REE mineralogy in HP–LT metapelites of the Sebtide complex, Rif,
596 Morocco: Monazite stability and geochronology. Lithos 87, 214–234.

597 Janots, E., Engi, M., Berger, A., Allaz, J., Schwarz, J.-O., and Spandler, C. (2008). Prograde
598 metamorphic sequence of REE minerals in pelitic rocks of the Central Alps: implications
599 for allanite-monazite-xenotime phase relations from 250 to 610 degrees C. J. Metamorph.
600 Geol. 26, 509–526.

601 Janots, E., Berger, A., and Engi, M. (2011). Physico-chemical control on the REE minerals in
602 chloritoid-grade metasediments from a single outcrop (Central Alps, Switzerland). Lithos
603 121, 1–11.

604 Janots, E., Berger, A., Gnos, E., Whitehouse, M., Lewin, E., and Pettke, T. (2012).
605 Constraints on fluid evolution during metamorphism from U–Th–Pb systematics in Alpine
606 hydrothermal monazite. Chem. Geol. 326–327, 61–71.

607 Kelly, N.M., Harley, S.L., and Möller, A. (2012). Complexity in the behavior and
608 recrystallization of monazite during high-T metamorphism and fluid infiltration. Chem.
609 Geol. 322-323:192–208.

610 Kirkland, C.L., Erickson, T.M., Johnson, T.E., Danišík, M., Evans, N.J., Bourdet, J., and
611 McDonald, B.J. (2016). Discriminating prolonged, episodic or disturbed monazite age
612 spectra: An example from the Kalak Nappe Complex, Arctic Norway. Chem. Geol.
613 424:96–110.

614 Kogawa, M., Watson, E.B., Ewing, R.C., and Utsunomiya, S. (2012). Lead in zircon at the
615 atomic scale. Am. Miner., 97, 1094-1102.

616 Kramers, J., Frei, R., Newville, M., Kober, B., and Villa, I. (2009). On the valency state of
617 radiogenic lead in zircon and its consequences. Chem. Geol., 261, 4-11.

618 Krenn, E., Putz, H., Finger, F., and Paar, W.H. (2011). Sulfur-rich monazite with high
619 common Pb in ore-bearing schists from the Schellgaden mining district (Tauern Window,
620 Eastern Alps). Mineral. Petrol. 102:51–62.

621 Kusiak, M.A., Dunkley, D.J., Wirth, R., Whitehouse, M.J., Wilde, S.A., and Marquardt, K.
622 (2015). Metallic lead nanospheres discovered in ancient zircons. PNAS, 112, 4958-4963.

623 Kusiak, M.A., Whitehouse, M.J., Wilde, S.A., Nemchin, A.A., and Clark, C. (2013).
624 Mobilization of radiogenic Pb in zircon revealed by ion imaging: Implications for early
625 Earth geochronology. Geology, 41, 291-294.

626 Laurent AT, Seydoux-Guillaume AM, Duchene S., Bingen B., Bosse V., and Datas L. (2016).
627 Sulphate incorporation in monazite lattice and dating the cycle of sulphur in metamorphic
628 belts. Contrib. Miner. Petrol., DOI 10.1007/s00410-016-1301-5.

629 Lee, J.K.W., Williams, I.S., and Ellis, D.J. (1997). Pb, U and Th diffusion in natural zircon.
630 Nature 390, 159–162.

631 Marsh, J.H., and Stockli, D.F. (2015). Zircon U–Pb and trace element zoning characteristics
632 in an anatectic granulite domain: Insights from LASS-ICP-MS depth profiling: Lithos,
633 239, 170-185.

634 McFarlane, C. R., and McKeough, M. (2013). Petrogenesis of the Kulyk Lake monazite-
635 apatite-Fe (Ti)-oxide occurrence revealed using in-situ LA-(MC)-ICP-MS trace element
636 mapping, U-Pb dating, and Sm-Nd isotope systematics on monazite. Am. Miner., 98,
637 1644-1659.

638 Meldrum, A., Boatner, L.A.,Weber,W.J., Ewing, R.C. (1998). Radiation damage in zircon and
639 monazite. Geochim. Cosmochim. Acta, 62, 2509–2520.

640 Montel, J.-M., Devidal, J.-L., and Avignant, D. (2002). X-ray diffraction study of brabantite-
641 monazite solid solution. Chem. Geol., 191:89-104.

642 Moser, D.E., Davis, W.J., Reddy, S.M., Flemming, R.L., and Hart, R.J. (2009). Zircon U-Pb
643 strain chronometry reveals deep impact triggered flow: Earth Planet. Sci. Lett., 277, 73-79.

644 Muhling, J.R., Fletcher, I.R., Rasmussen, B. (2012). Dating fluid flow and Mississippi Valley
645 type base-metal mineralization in the Paleoproterozoic Earaheedy Basin, Western
646 Australia. Precambrian Res., 212-213, 75-90.

Nasdala, L., Hanchar, J.M., Rhede, D., Kennedy, A.K., Váczi, T. (2010). Retention of uranium in complexly altered zircon: an example from Bancroft, Ontario. Chem. Geol., 269, 290-300.

Nemchin, A.A., Horstwood, M.S.A., and Whitehouse, M.J. (2013). High-spatial-Resolution Geochronology. Elements, 9, 31-37.

Ni, Y., Hughes, J.M., and Mariano, A.N. (1995). Crystal chemistry of the monazite and xenotime structures. Am. Mineral., 80, 21-26.

Ondrejka, M., Uher, P., Pršek, J., Ozdín, D. (2007). Arsenian monazite-(Ce) and xenotime-(Y), REE arsenates and carbonates from the Tisovec-Rejkovo rhyolite, Western Carpathians, Slovakia: Composition and substitutions in the (REE,Y)XO_4 system (X = P, As, Si, Nb, S). Lithos, 95, 116-129.

Parrish, R.R. (1990). U–Pb dating of monazite and its application to geological problems. Can. J. Earth Sci., 27, 1431-1450.

Peterman, E.M., Reddy, S.M., Saxey, D.W., Snoeyenbos, D.R., Rickard, W.D.A., Fougerouse, D., and Kylander-Clark, A.R.C. (2016). Nanogeochronology of discordant zircon measured by atom probe microscopy of Pb-enriched dislocation loops. Sci. Adv., 2016, 2: e1601318.

Piazolo, S., La Fontaine, A., Trimby, P., Harley, S., Yang, L., Armstrong, R., and Cairney, J. M. (2016). Deformation induced trace element redistribution in zircon revealed using atom probe tomography. Nat. Commun. 7, 10490.

Pidgeon RT, O'Neil JR, and Silver RT (1995). The interdependence of U-Pb stability, crystallinity and external conditions in natural zircons - an early experimental study. In: Leon T. Silver 70th Birthday Symposium and Celebration, Extended Abstracts, 225-231.

Pidgeon, R. (2014). Zircon radiation damage ages. Chem. Geol., 367, 13-22.

Pidgeon, R.T., O'Neil, J.R., and Silver, R.T. (1966). Uranium and lead isotopic stability in a metamict zircon under experimental hydrothermal conditions. Science, 154, 1538-1540.

Poitrasson, F., Chenery, S., Bland, D.J. (1996): Contrasted monazite hydrothermal alteration mechanisms and their geochemical implications for the U-Th-Pb geochronology and nuclear ceramics. Earth Planet. Sci. Let., 145, 79-96.

675 Poitrasson, F., Chenery, S., Shepherd, T.J. (2000): Electron microprobe and LA-ICP-MS
676 study of monazite hydrothermal alteration: implications for the U-Th-Pb geochronology
677 and nuclear ceramics. Geochim. Cosmochim. Acta, 64, 3283-3297.

678 Prsek, J., Ondrejka, M., Bacik, P., Budzyn, B., and Uher, P. (2010). Metamorphic-
679 hydrothermal REE minerals in the Bacuch magnetite deposit, Western Carpathians,
680 Slovakia: (S, Sr)-rich monazite-(Ce) and Nd-dominant hingganite. Can. Mineral., 48, 81-
681 94.

682 Putnis, A. (2009). Mineral replacement reactions. Reviews in Mineralogy and Geochemistry,
683 70, 87-124.

684 Putnis, A., and Putnis, C.V. (2007). The mechanism of reequilibration of solids in the
685 presence of a fluid phase. J. Solid State Chem. 180, 1783–1786.

686 Pyle, J.M., Spear, F.S., Rudnick, R.L., and McDonough, W.F. (2001). Monazite-xenotime-
687 garnet equilibrium in metapelites and a new monazite-garnet thermometer. J. Petrol., 42,
688 2083-2107.

689 Rasmussen, B., and Muhling, J.R. (2007). Monazite begets monazite: evidence for dissolution
690 of detrital monazite and reprecipitation of syntectonic monazite during low-grade regional
691 metamorphism. Contrib. Mineral. Petrol., 154, 675-689.

692 Rasmussen, B., Fletcher, I.R., and McNaughton, N.J. (2001). Dating low-grade metamorphic
693 events by SHRIMP U-Pb analysis of monazite in shales. Geology, 29, 963-966.

694 Rasmussen, B., Fletcher, I.R., Muhling, J.R., Gregory, C.J., and Wilde, S.A. (2011).
695 Metamorphic replacement of mineral inclusions in detrital zircon from Jack Hills,
696 Australia: Implications for the Hadean Earth. Geology, 39, 1143-1146.

697 Rubatto, D., Williams, S.I., and Buick, S.I. (2001). Zircon and monazite response to prograde
698 metamorphism in the Reynolds Range, central Australia. Contrib. Mineral. Petrol. 140,
699 458–468. doi:10.1007/PL00007673

700 Rubatto, D., Chakraborty, S., and Dasgupta, S. (2013). Timescales of crustal melting in the
701 Higher Himalayan Crystallines (Sikkim, Eastern Himalaya) inferred from trace element-
702 constrained monazite and zircon chronology. Contrib. Mineral. Petrol. 165, 349–372.

703 Salje, E.K.H., Chrosch, J., and Ewing, R.C. (1999). Is “metamictization” of zircon a phase
704 transition? Am. Mineral., 84, 1107-1116.

705 Schoene, B., Condon, D.J., Morgan, L. and McLean, N. (2013). Precision and Accuracy in
706 Geochronology. Elements, 9, 19-24.

707 Seydoux-Guillaume, A.M., Bingen, B., Paquette, J.L., and Bosse, V. (2015). Nanoscale
708 evidence for uranium mobility in zircon and the discordance of U–Pb chronometers. Earth
709 Planet. Sci. Lett., 409, 43-48.

710 Seydoux-Guillaume, A.-M., Goncalves, P., Wirth, R., and Deutsch, A. (2003). Transmission
711 electron microscope study of polyphase and discordant monazites: Site-specific specimen
712 preparation using the focused ion beam technique. Geology 31, 973–976.

713 Seydoux-Guillaume, A.-M., Montel, J.-M., Bingen, B., Bosse, V., de Parseval, P., Paquette,
714 J.-L., Janots, E., Wirth, R. (2012). Low-temperature alteration of monazite: Fluid mediated
715 coupled dissolution–precipitation, irradiation damage, and disturbance of the U–Pb and
716 Th–Pb chronometers. Chem Geol, 330-331:140–158.

717 Seydoux-Guillaume, A.-M., Paquette, J.-L., Wiedenbeck, M., Montel, J.-M., and Heinrich, W.
718 (2002a). Experimental resetting of the U–Th–Pb systems in monazite. Chem Geol,
719 191:165–181.

720 Seydoux-Guillaume, A.M., Wirth, R., and Ingrin, J. (2007). Contrasting response of $ThSiO_4$
721 and monazite to natural irradiation. Eur. J. Mineral., 19, 7-14.

722 Seydoux-Guillaume, A.M., Wirth, R., Deutsch, A., and Schärer, U. (2004). Microstructure of
723 24-1928 Ma concordant monazites: implications for geochronology and nuclear waste
724 deposits. Geoch. Cosmochim. Acta, 68, 2517-2527.

725 Seydoux-Guillaume, A.-M., Wirth, R., Heinrich, W., and Montel, J.-M. (2002b).
726 Experimental determination of the Th partitioning between monazite and xenotime using
727 Analytical Electron Microscopy and X-ray Diffraction Rietveld analysis. Eur. J. Mineral.,
728 14, 869-878.

729 Shazia, J.R., Harlov, D.E., Suzuki, K., Kim, S.W., Girish-Kumar, M., Hayasaka, Y., Ishwar-
730 Kumar, C., Windley, B.F., and Sajeev, K. (2015). Linking monazite geochronology with
731 fluid infiltration and metamorphic histories: Nature and experiment. Lithos 236–237, 1–15.

732 Sinha, A.K., Wayne, D.M, and Hewitt, D.A. (1992). The hydrothermal stability of zircon:
733 preliminary experimental and isotopic studies. Geochim. Cosmochim. Acta, 56, 3535-
734 3551.

735 Spear, F.S., and Pyle, J.M. (2002). Apatite, Monazite, and Xenotime in metamorphic rocks. In
736 Reviews in Mineralogy and Geochemistry (ed. P. H. Ribbe) 48, pp. 293-335.
737 Mineralogical Society of America.

738 Tanaka, K., Takahashi, Y., Horie, K., Shimizu, H., and Murakami, T. (2010). Determination
739 of the oxidation state of radiogenic Pb in natural zircon using X-ray absorption near-edge
740 structure. Phys. Chem. Miner., 37, 249-254.

741 Teufel, S., and Heinrich, W. (1997). Partial resetting of the U–Pb isotope system in monazite
742 through hydrothermal experiments: an SEM and U–Pb isotope study. Chem. Geol., 137,
743 273-281.

744 Trachenko, K., Dove, M.T., and Salje, E.K.H. (2003). Structural changes in zircon under α-
745 decay irradiation. Phys. Rev., 65, 180102(R).

746 Utsunomiya, S., Palenik, C.S., Valley, J.W., Cavosie, A.J., Wilde, S.A., Ewing, R.C. (2004).
747 Nanoscale occurrence of Pb in an Archean zircon. Geochim. Cosmochim. Acta, 68, 4679-
748 4686.

749 Utsunomiya, S., Valley, J.W., Cavosie, A.J., Wilde, S.A., and Ewing, R.C. (2007). Radiation
750 damage and alteration of zircon from a 3.3 Ga porphyritic granite from the Jack Hills,
751 Western Autralia. Chem. Geol., 236, 92-111.

752 Valley, J.W., Cavosie, A.J., Ushikubo, T., Reinhard, D.A., Lawrence, D.F., Larson, D.J.,
753 Clifton, P.H., Kelly, T.F., Wilde, S.A., Moser, D.E., Spicuzza, M.J. (2014). Hadean age for
754 a post-magma-ocean zircon confirmed by atom-probe tomography. Nat. Geosci.,7, 219-
755 223.

756 Valley, J. W., Reinhard, D.A., Cavosie, A.J., Ushikubo, T., Lawrence, D.F., Larson, D.J.,
757 Kelly, T.F., Snoeyenbos, D.R., and Strickland, A. (2015). Nano-and micro-geochronology
758 in Hadean and Archean zircons by atom-probe tomography and SIMS: New tools for old
759 minerals. Am. Mineral. 100, 1355-1377.

760 Villa, I.M., and Williams, M.L. (2013). Geochronology of metasomatic events. In: Harlov D
761 & Austrheim H (eds) Metasomatism and the Chemical Transformation of Rock: the role of
762 fluids in terrestrial and extraterrestrial processes. Springer, Berlin, pp 171-202.

763 Wang, J.-M., Rubatto, D., and Zhang, J.-J. (2015). Timing of Partial Melting and Cooling
764 across the Greater Himalayan Crystalline Complex (Nyalam, Central Himalaya): In-
765 sequence Thrusting and its Implications. J. Petrol. 56, 1677–1702.

766 Wawrzenitz, N., Krohe, A., Rhede, D., and Romer, R.L. (2012). Dating rock deformation
767 with monazite: The impact of dissolution precipitation creep. Lithos, 134-135, 52-74.

768 Whitehouse, M.J., Kumar, G.R.R., and Rimša, A. (2014). Behaviour of radiogenic Pb in
769 zircon during ultrahigh-temperature metamorphism: An ion imaging and ion tomography
770 case study from the Kerala Khondalite Belt, southern India. Contrib. Mineral. Petrol., 168,
771 1-18.

772 Whitney, J. (1984). Fugacities of sulfurous gases in pyrrhotite-bearing silicic magmas. Am.
773 Mineral., 69, 69–79.

774 Williams, M.L., Jercinovic, M.J., and Terry, M.P. (1999). Age mapping and dating of
775 monazite on the electron microprobe: Deconvoluting multistage tectonic histories.
776 Geology, 27, 1023-1026.

777 Williams, M.L., Jercinovic, M.J., and Hetherington, C.J. (2007). Microprobe Monazite
778 Geochronology: Understanding Geologic Processes by Integrating Composition and
779 Chronology. Annu. Rev. Earth Planet. Sci., 35, 137–175.

780 Williams, M.L., Jercinovic, M.J., Harlov, D.E., Budzyń, B., and Hetherington, C.J. (2011).
781 Resetting monazite ages during fluid-related alteration: Chem. Geol., 283, 218-225.

782 Williams, M.L., and Jercinovic, M.J. (2012). Tectonic interpretation of metamorphic
783 tectonites: integrating compositional mapping, microstructural analysis and in situ
784 monazite dating. J. Metamorph. Geol. 30, 739–752.

785 Wirth, R. (2004). Focused Ion Beam (FIB): a novel technology for advanced application of
786 micro- and nanoanalysis in geosciences and applied mineralogy. Eur. J. Mineral., 16, 863-
787 877.

788 Wirth, R. (2009). Focused Ion Beam (FIB) combined with SEM and TEM: advanced
789 analytical tools for studies of chemical composition, microstructure and crystal structure in
790 geomaterials on a nanometer scale. Chem. Geol., 261, 217-229.

791 Xu, X.S., Zhang, M., Zhu, K.Y., Chen, X.M., He, Z.Y. (2012). Reverse age zonation of zircon
792 formed by metamictisation and hydrothermal fluid leaching. Lithos150, 256–267.

793 Yakymchuk, C., and Brown, M. (2014). Behaviour of zircon and monazite during crustal
794 melting: J. Geol. Soc. London, 171, 465-479.

795

796 **Figure captions**

797 **Figure 1**

798 Transmission Electron Microscope (TEM) images from U- or Th-rich-nano-phases in various
799 accessory minerals. A-Bright-Field (BF) TEM and B-Dark-Field (DF) TEM images of
800 $ThSiO_4$ exsolutions (arrows) in apatite. C- Scanning TEM of uraninite (UO_2) nanocrystals
801 (arrow) in porous zircon crystal from the Evje-Iveland pegmatite field in Norway [modified
802 from Seydoux-Guillaume et al., 2015). D- BF-TEM of nano-crack filled with $ThSiO_4$ in
803 monazite (mnz) crystal from Madagascar [modified from Seydoux-Guillaume et al., 2012).
804 hmt: hematite.

805

806 **Figure 2**

807 A- Tera-Wasserburg Concordia diagram and B- $^{207}Pb/^{206}Pb$ ratio images of zircon grains from
808 sample 16178-2 from Napier complex, East Antarctica, analyzed using Secondary Ion Mass
809 Spectrometry (SIMS) [modified from Kusiak et al., 2013]. C- High Angle Annular Dark Field
810 (HAADF) TEM image and D- High Resolution TEM image of Pb nanosphere in zircon
811 crystal from the same sample [modified from Kusiak et al., 2015].

812

813 **Figure 3**

814 A- Tera-Wasserburg Concordia diagram for 9 zircon crystals included in plagioclase and in
815 xenotime crystals from the Evje-Iveland pegmatite field in Norway. Most points are scattering
816 along two discordia lines (blue for zircon included in plagioclase and yellow for zircon
817 included in xenotime) with intercepts having little geological significance. B- Back Scattered
818 Electron (BSE) image from one zircon (zrn) crystal included in plagioclase (plg) with position
819 extraction of the Focused Ion Beam (FIB) foil. C- STEM-HAADF image from FIB3 foil cut
820 from zircon crystal in B and the corresponding U-chemical map (D) showing close

association of UO_2 nanocrystals (bright points in C) within nanopores (black in C). Modified from Seydoux-Guillaume et al. [2015].

Figure 4

A- Weighted histogram of 448 Electron Microprobe (EPMA) chemical U–Th–Pb ages for 26 monazite crystals included in garnet, quartz and coronitic textures from the Andriamena unit in Madagascar. B- BF-TEM image of FIB foil cut in monazite core showing EPMA age dispersion (911-1805 Ma). Note dark domains 2, with one in a nano-pore that probably correspond to fluid inclusion. Monazite matrix (1) revealed also typical mottled diffraction contrasts due to distorted volumes in monazite lattice in response to radiation damage. C: Overlay of analysis of monazite matrix (1) and representative Energy Dispersive X-Ray (EDS) analysis of dark domain (2) in B. Compared to monazite matrix, dark domains are very enriched in Pb and, to lesser extent, in Ca and Si. REE—rare earth elements. Modified from Seydoux-Guillaume et al. [2003].

Figure 5

A- EPMA dating in mnz1 (554 ± 11 Ma) and altered rims (alt mnz in B) of monazite grains altered at 500°C (B). In altered domains, ages spread in the range of 40–440 Ma, with a weighted average age of 163 ± 54 Ma, due to incomplete replacement of mnz1 by a secondary monazite (mnz2) within the altered rim and the analysis of a nano-mixture of different proportions of mnz1 vs mnz2 in the analyzed volume (C). MSWD—mean square of weighted deviates. B- BSE image of monazite grain altered during an hydrothermal experiment at 500°C, 2 kbar, 114 days with NaOH (1M), and mounted in epoxy. alt mnz: domain of the monazite grain that has been altered during experiment; mnz1: unreacted grain. FIB: location of the foil seen in C. C- STEM-HAADF image of FIB foil cut from B. Dash line show the interaction domain when using EPMA analyses (25 kV). mnz2: secondary monazite, free of Pb, formed during experiment and only visible at the nanoscale. Pt: platinum deposit for FIB preparation. Modified from Grand'homme et al. [2016b].

Figure 6

A- BSE image from one monazite grain with 3 domains (D1-D3) defined by different compositions. D1: S-rich (0.45–0.72 Wt. % SO2) monazite core with Th incorporated as cheralite [$CaTh(PO_4)_2$] component; D2: S-bearing domain (SO_2> 0.05 Wt.%) partly clouded with solid inclusions (black points in A) and D3: S-free, Y and Th-rich domains with Th accommodated as huttonite ($ThSiO_4$) component. FIB foil (E-F) was cut in domain D1. B-D U–Pb data presented in Tera-Wasserburg plots. B– all analyses. C–all analyses with colour coding corresponding to SiO_2 concentrations (in Wt.%) measured by EPMA prior to laser ablation. D– Same figure with color coding for SO_2 concentrations. E-F: STEM-HAADF images of foil cut in D1 (A). E- low magnification image reveals black dots (1) corresponding to negative density contrasts in monazite core D1 (2). EDS analysis demonstrated that they correspond to $CaSO_4$-rich nanocluster (not shown). F- High-resolution image in zone axis [101] of one $CaSO_4$ nanocluster (~5-10 nm) in monazite lattice. Bright spots in E corresponds to Ga implantation during sample preparation.

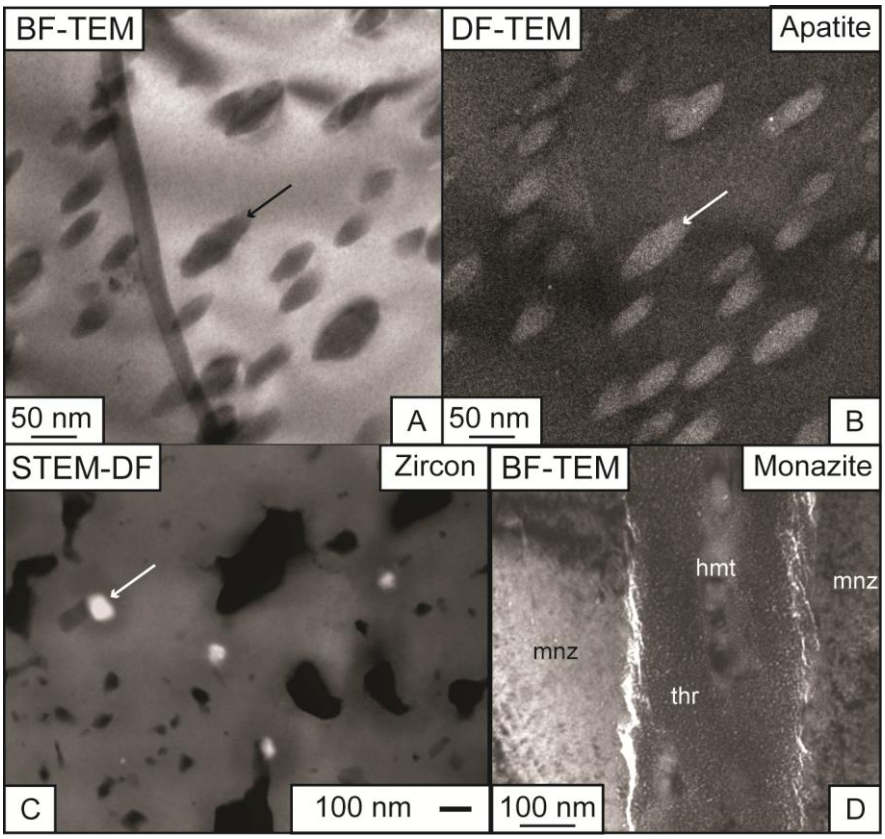

866

867 Figure 1

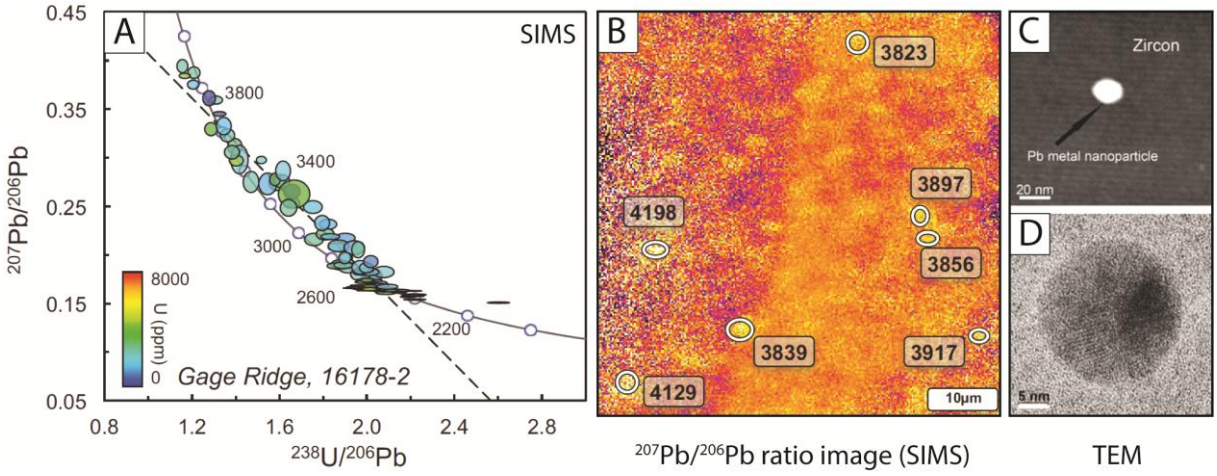

868

869 Figure 2

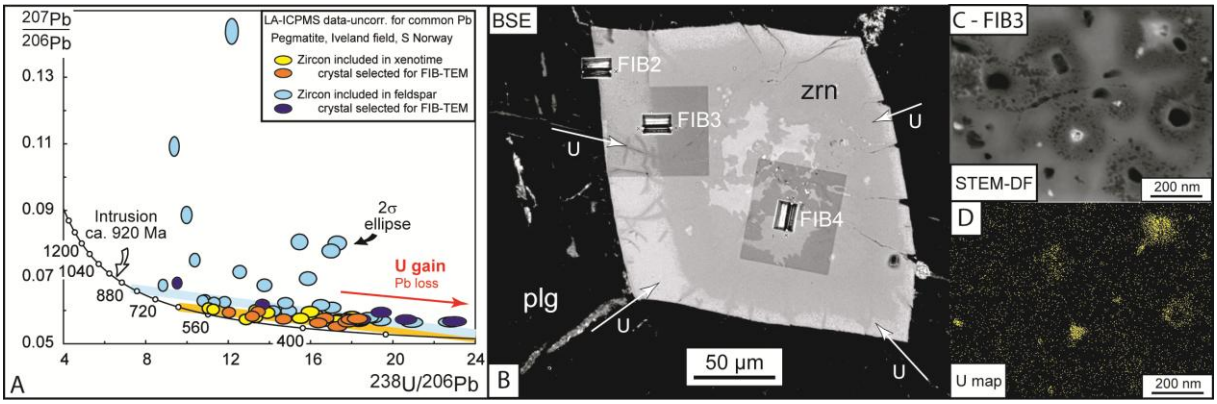

870

871 Figure 3

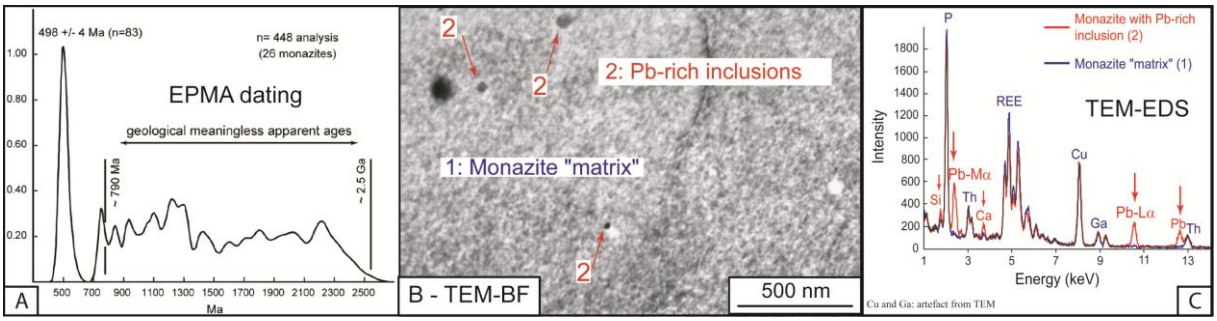

872

873 Figure 4

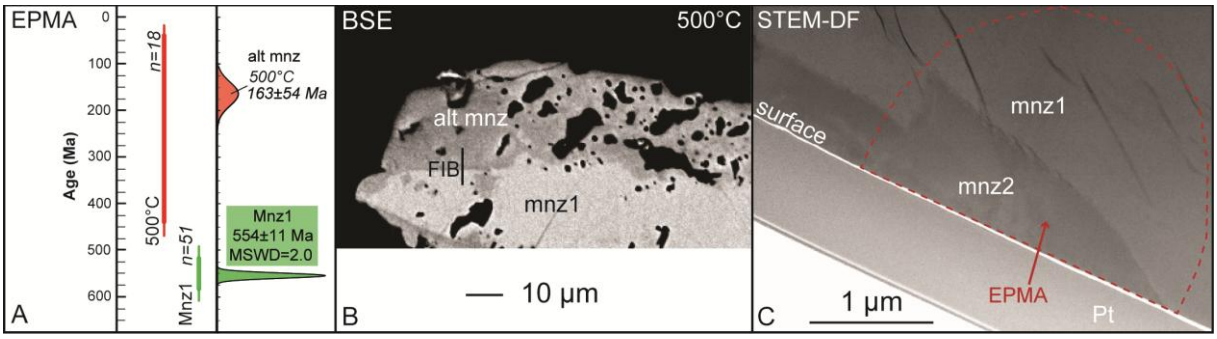

874

875 Figure 5

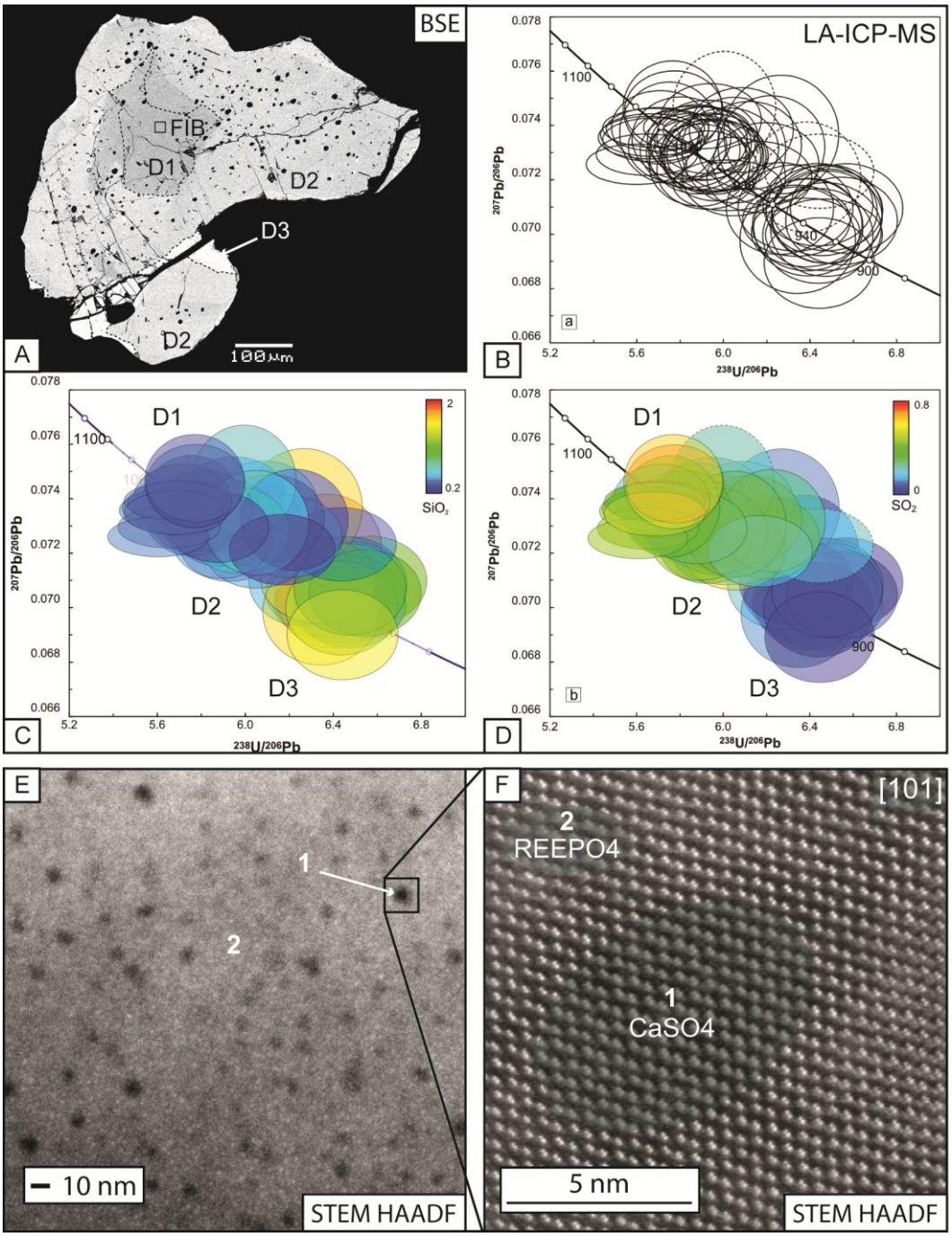

876

877 Figure 6